BeBeC-2026-S04

Order-selective beamforming via block-wise pre-CSM filtering

Christof Puhle
puhle@gfai.de
Society for the Advancement of Applied Computer Science (GFaI) e.V.
Volmerstr. 3, 12489 Berlin, Germany

Abstract

This paper presents a computationally efficient and novel method for isolating acoustic orders from microphone array measurements synchronized with rotational speed (RPM) data, enabling high-resolution frequency-domain beamforming for precise acoustic source localization. Traditional order-tracking and beamforming techniques either rely on resampling, which introduces artifacts, or fail to adapt to variable RPM conditions, resulting in blurred acoustic maps and reduced accuracy.

Our approach, applied as an order-selective preprocessing step prior to cross-spectral matrix (CSM) construction, yields block-wise spectral representations that remain consistent under nonstationary operating conditions. Without requiring explicit knowledge of the instantaneous order frequency in the frequency domain, the filtered data can then be processed using advanced frequency-domain beamforming techniques (e.g., CLEAN-SC) to produce high-resolution acoustic maps.

Comparative evaluations of existing order-tracking techniques, such as computed order tracking (COT) and Vold-Kalman filtering (VKF), demonstrate improved spectral consistency and robustness. The proposed approach is further applied to both simulated and real-world measurement scenarios, where it enables improved interpretability when combined with advanced frequency-domain beamforming methods.

The method's low computational overhead makes it well-suited for industrial applications, including rotating machinery diagnostics and reliable noise source identification.

1 Introduction

Order-tracking techniques are widely used for the analysis of rotational machinery under non-stationary operating conditions [3, 5, 8, 12]. In particular, computed order tracking (COT) and Vold-Kalman filtering (VKF) provide effective means to extract rotation-synchronous components from time-domain measurements [6, 9, 12]. These methods are commonly applied prior to acoustic analysis or combined with beamforming approaches for source localization [4, 10].

However, conventional workflows typically perform beamforming either in the time domain or after reconstructing time-domain order components over the entire measurement duration [10, 13]. This can lead to limitations when dealing with strongly nonstationary signals, closely spaced orders, or complex multi-source environments. In particular, the resulting spatial maps may suffer from leakage, artefacts, or misleading interpretations due to sidelobes.

In this paper, we propose a novel and block-wise order-tracking framework that directly yields localized spectral representations suitable for cross-spectral matrix (CSM) construction. The resulting order-selective pre-CSM filtering enables robust integration with frequency-domain beamforming methods, without requiring explicit knowledge of the instantaneous frequency of the target order.

The proposed method is validated using both a controlled simulation and a real-world measurement. We demonstrate that, while conventional methods may yield visually plausible results, the combination of the proposed method with advanced CSM-based techniques such as CLEAN-SC provides more reliable and physically consistent source reconstructions.

The paper is structured as follows: section 2 describes the simulation setup used to compare the baseline order-tracking methods introduced in subsection 3.1 with the proposed method presented in subsection 3.2. The results of this comparison are given in subsection 3.3. Finally, subsection 4.3 presents beamforming results using the proposed method as a pre-CSM filtering approach (cf. subsection 4.2). Both simulation and real-world measurement scenarios are considered, and the results are compared with time-domain beamforming using revolution-synchronous resampling (see subsection 4.1).

2 Simulation procedure

This section describes the complete simulation procedure used to (i) generate a non-stationary rotational reference (including run-up/run-down, ripple, jitter and sharp transients), (ii) synthesize a microphone time signal from a known analytic target order component and multiple realistic disturbances (close-by orders, harmonics, stationary tones, colored noise and impulses), and (iii) provide a ground truth for quantitative error assessment and runtime benchmarking (see subsection 3.3) of order-tracking pipelines (i.e. VKF, COT, and our proposed method).

2.1 Sampling, duration and notation

Let the discrete time axis be $t_n = n/f_s$, $n = 0,\dots,N-1$, where $f_s = 48\,000\,\mathrm{Hz}$ is the sampling rate and $N = \lfloor T f_s \rfloor$ is the number of samples for a measurement duration of $T = 4\,\mathrm{s}$. Unless stated otherwise, all signals are real-valued.

2.2 Non-trivial rotational speed signal

The rotational reference is synthesized as a run-up and run-down profile with superimposed periodic ripple, stochastic jitter, and a localized transient dip. This combination is intended to emulate realistic speed sweeps with control-loop oscillations and measurement noise [8].

RPM profile. A smooth run-up and run-down between

$$\mathrm{rpm}_{\min} = 1000\,\mathrm{min}^{-1} \tag{1}$$

and

$$\mathrm{rpm}_{\max} = 4000\,\mathrm{min}^{-1} \tag{2}$$

is generated using the following cosine-based profile:

$$p(t) = \frac{1}{2}\left(1 - \cos\left(2\pi\frac{t}{T}\right)\right), \tag{3}$$

$$\mathrm{rpm}_{\mathrm{nom}}(t) = \mathrm{rpm}_{\min} + (\mathrm{rpm}_{\max} - \mathrm{rpm}_{\min})\; p(t), \tag{4}$$

which yields a smooth acceleration and deceleration with zero slope at the start and end.

Periodic ripple. To model small periodic speed modulations (e.g. due to load oscillations or closed-loop control), a ripple component is added:

$$\mathrm{rpm}_{\mathrm{rip}}(t) = A_1 \sin(2\pi f_1 t) + A_2 \sin(2\pi f_2 t + \varphi_2), \tag{5}$$

with amplitudes $A_1 = 40\,\mathrm{min}^{-1}$ and $A_2 = 20\,\mathrm{min}^{-1}$, frequencies $f_1 = 1.0\,\mathrm{Hz}$ and $f_2 = 2.7\,\mathrm{Hz}$ and a phase offset of $\varphi_2 = 1.1$ between both components.

Random-walk jitter. Tachometer or estimated RPM often exhibits low-frequency drift. We simulate this by a discrete Gaussian random walk:

$$\mathrm{rpm}_{\mathrm{jit}}(t) = \sum_{i=0}^{\lfloor t f_s \rfloor} \eta_i, \qquad \eta_i \sim \mathcal{N}(0, \sigma_\eta^2), \tag{6}$$

where the standard deviation $\sigma_\eta = 0.08$ controls the jitter magnitude.

Transient dip. Finally, a localized speed perturbation (e.g. short torque transient) is modeled by a Gaussian dip:

$$\mathrm{rpm}_{\mathrm{tr}}(t) = -A_{\mathrm{tr}} \exp\left(-\frac{(t - t_0)^2}{2\sigma_{\mathrm{tr}}^2}\right). \tag{7}$$

Its amplitude is fixed as $A_{\mathrm{tr}} = 250\,\mathrm{min}^{-1}$ centered at $t_0 = 0.55T$ with a width of $\sigma_{\mathrm{tr}} = 0.04T$. For $T = 4\,\mathrm{s}$ this corresponds to $t_0 = 2.2\,\mathrm{s}$ and $\sigma_{\mathrm{tr}} = 0.16\,\mathrm{s}$.

Final RPM signal. The complete non-trivial RPM reference is

$$\mathrm{rpm}(t) = \mathrm{rpm}_{\mathrm{nom}}(t) + \mathrm{rpm}_{\mathrm{rip}}(t) + \mathrm{rpm}_{\mathrm{jit}}(t) + \mathrm{rpm}_{\mathrm{tr}}(t). \tag{8}$$

2.3 Rotational phase from RPM

Order-related components are defined via the accumulated rotational phase. The instantaneous rotational frequency is

$$f_r(t) = \frac{\mathrm{rpm}(t)}{60}. \tag{9}$$

The rotational phase is the integral

$$\phi(t) = 2\pi \int_0^t f_r(\tau)\, d\tau, \tag{10}$$

approximated in discrete time by the sum

$$\phi(t_n) \approx 2\pi \sum_{i=0}^{n-1} \frac{f_r(t_i)}{f_s}. \tag{11}$$

This phase serves as the common reference for defining order components and for applying order-tracking algorithms.

2.4 Analytic target order component (ground truth)

To enable quantitative error evaluation, the target order component is synthesized analytically. We begin by defining a slowly modulated amplitude

$$a(t) = 1 + a_1 \sin(2\pi f_{a_1} t) + a_2 \sin(2\pi f_{a_2} t + \varphi_{a_2}), \tag{12}$$

with modulation frequencies $f_{a_1} = 0.6\,\mathrm{Hz}$, $f_{a_2} = 1.4\,\mathrm{Hz}$ and amplitudes $a_1 = 0.35$, $a_2 = 0.2$, respectively, the second term is furnished with a constant phase offset, $\varphi_{a_2} = 0.3$. The analytic complex envelope is then chosen as

$$a_{\mathrm{true}}(t) = a(t)\, e^{j\varphi_0}, \quad \varphi_0 = 0.7. \tag{13}$$

Finally, for a fixed order of $\kappa_0 = 100$, the real-valued target order time signal is

$$x_{\mathrm{true}}(t) = \Re\left\{ a_{\mathrm{true}}(t)\, e^{j\kappa_0 \phi(t)} \right\} = a(t) \cos(\kappa_0 \phi(t) + \varphi_0)\,. \tag{14}$$

In the later discussion, the order-tracked outputs $\hat{x}$ and the estimated envelopes $\hat{a}$ can be compared directly against this analytic ground truth.

2.5 Interfering components and disturbances

The microphone signal includes additional components to make the benchmark non-trivial and to stress selectivity, leakage and robustness.

Nearby interfering order. To test the ability to separate close orders, an interferer at a neighboring order k_1 is added,

$$x_{\text{int}}(t) = a_{\text{int}} \cos(\kappa_1 \phi(t) + \varphi_{\text{int}}), \qquad \kappa_1 = \kappa_0 + 0.125, \tag{15}$$

chosen such that leakage and partial overlap is plausible, and

$$a_{\text{int}} = 0.5, \quad \varphi_{\text{int}} = 1.0. \tag{16}$$

Harmonic order. A weaker harmonic at order $2\kappa_0$ models the influence of higher harmonics:

$$x_{\text{harm}}(t) = a_{\text{harm}} \cos(2\kappa_0 \phi(t) + \varphi_{\text{harm}}), \quad a_{\text{harm}} = 0.2, \quad \varphi_{\text{harm}} = 0.4. \tag{17}$$

Stationary sinusoid. To emulate unrelated tonal noise not tied to RPM, a stationary sinusoid is added:

$$x_{\text{stat}}(t) = a_{\text{stat}} \cos(2\pi f_{\text{stat}} t + \varphi_{\text{stat}}), \tag{18}$$

where f_{stat} is fixed at 4000 Hz, and $a_{\text{stat}} = 0.2$, $\varphi_{\text{stat}} = 0.2$.

Colored and broadband noise. To represent realistic background noise, a band-limited colored noise component is generated by filtering white Gaussian noise w with a 3rd-order Butterworth band-pass h_{bp} from 200 Hz to 4000 Hz and scaling by $a_{\text{col}} = 0.3$:

$$x_{\text{col}}(t) = a_{\text{col}} (h_{\text{bp}} * w)(t), \qquad w(t) \sim \mathcal{N}(0,1), \tag{19}$$

where zero-phase filtering is used to avoid additional phase distortion.

Impulsive disturbances. To stress robustness against clicks/outliers, six short impulses are injected at selected time instants

$$\tau_i = 1\,\text{s} + i \cdot 0.4\,\text{s}, \quad i = 0, \ldots, 5. \tag{20}$$

Each impulse uses the 8-sample waveform

$$q = (1, -0.8, 0.6, -0.4, 0.25, -0.15, 0.1, -0.05) \tag{21}$$

scaled by $a_{\text{imp}} = 0.35$ and is injected starting at sample index $n_i = \lfloor \tau_i f_s \rfloor$:

$$x_{\text{imp}}(t) = a_{\text{imp}} \sum_{i=0}^{5} \sum_{j=0}^{7} q_j \delta_{\lfloor t f_s \rfloor - (n_i + j)}. \tag{22}$$

Physical baseline (pre-sensor). The baseline signal prior to sensor effects therefore is

$$x_{\text{base}}(t) = x_{\text{true}}(t) + x_{\text{int}}(t) + x_{\text{harm}}(t) + x_{\text{stat}}(t) + x_{\text{col}}(t) + x_{\text{imp}}(t). \tag{23}$$

2.6 Sensor-channel effects and final simulated measurement

A simple sensor/channel model is applied to emulate sensitivity variation, a phase-like mismatch parameter and additive self-noise:

$$g \sim \mathscr{U}(0.8, 1.2), \qquad \psi \sim \mathscr{U}(-0.5, 0.5), \qquad \nu(t) \sim \mathscr{N}(0, 0.08^2). \tag{24}$$

The final simulated microphone signal is

$$x_{\mathrm{sim}}(t) = g\cos(\psi)\, x_{\mathrm{base}}(t) + \nu(t). \tag{25}$$

2.7 Reproducibility

All stochastic components (jitter, noise, sensitivity variation and phase-like mismatch) are driven by a fixed pseudo-random seed to ensure bitwise reproducibility of the simulated dataset. In the comparison below, all order-tracking methods process the same measured signal $x_{\mathrm{sim}}(t)$. This enables us to evaluate the resulting order-tracked signals $\hat{x}(t)$ and estimated envelopes $\hat{a}(t)$ against the analytic ground truth $\big(x_{\mathrm{true}}(t), a_{\mathrm{true}}(t)\big)$, and to rank the methods consistently using the same error metrics.

3 Order tracking

3.1 State-of-the-art order tracking baselines

To benchmark the proposed order-tracking method, we consider two established variable-speed order extraction methods: (i) computed order tracking (COT) via synchronous resampling and (ii) Vold–Kalman order tracking (VKF).

Computed order tracking (COT) via synchronous resampling

Computed order tracking transforms a time-sampled signal $x(t)$ into an angle-domain signal $\bar{x}(\alpha)$ sampled at constant angular increments, such that rotation-synchronous components become stationary with respect to α and can be analyzed by FFT methods in the order domain [9]: As before, let the instantaneous rotational speed be $f_r(t) = \mathrm{rpm}(t)/60$ and the accumulated phase be

$$\alpha(t) \equiv \phi(t) = 2\pi \int_0^t f_r(\tau)\, d\tau. \tag{26}$$

In the first step, COT constructs a uniform angle grid

$$\alpha_i = \alpha_0 + i\Delta\alpha, \quad \alpha_0 = \alpha(t_0) = 0, \quad \alpha_{N_\alpha - 1} = \alpha(t_{N-1}), \quad \Delta\alpha = \frac{2\pi}{360}, \quad i = 0, \ldots, N_\alpha - 1, \tag{27}$$

and determines the corresponding (generally non-uniform) time instants $\bar{t}_i$ such that $\alpha(\bar{t}_i) = \alpha_i$. In practice, $\bar{t}_i$ is obtained by interpolation of the estimated angle-time relation Equation 11. A second interpolation step then yields the angle-domain signal

$$\bar{x}(\alpha_i) = \bar{x}(\alpha(\bar{t}_i)) \triangleq x(\bar{t}_i) \approx \mathrm{interp}\big(x(t), \bar{t}_i\big). \tag{28}$$

To isolate an order κ_0, COT then applies complex demodulation:

$$z(\alpha_i) = \bar{x}(\alpha_i)\, e^{-j\kappa_0\alpha_i}. \tag{29}$$

This shifts the spectral content around order κ_0 to baseband (near zero order). A low-pass filter h_{LP} in the angle domain then retains only the desired order band while ideally suppressing other orders:

$$\tilde{z}(\alpha_i) = (h_{\mathrm{LP}} * z)(\alpha_i), \tag{30}$$

where the cutoff is chosen according to the intended half-bandwidth $\Delta\kappa$ in orders. Finally, the selected component is shifted back to its original order location by remodulation, yielding the order-filtered signal in the angle domain:

$$\tilde{x}(\alpha_i) = \Re\left\{2\,\tilde{z}(\alpha_i)\, e^{j\kappa_0\alpha_i}\right\}. \tag{31}$$

The factor 2 compensates the $1/2$ amplitude of the analytic (one-sided) representation created when demodulating a real-valued signal. For an order band $\kappa \in [\kappa_a, \kappa_b]$, de- and remodulation is performed at the center order $\kappa_{center} = (\kappa_a + \kappa_b)/2$ and the low-pass cutoff is set to cover $\Delta\kappa = (\kappa_b - \kappa_a)/2$. To reconstruct the time-domain signal $\hat{x}(t)$ on the original uniform grid $t_n = n/f_s$, COT interpolates the relation $(\bar{t}_i, \tilde{x}(\alpha_i))$ to obtain $\hat{x}(t_n)$.

COT is attractive for its conceptual simplicity and direct mapping to order spectra; however, accuracy depends on the quality of the speed/phase estimate, interpolation scheme and pulses-per-revolution [9].

Vold-Kalman order tracking filter (VKF)

The Vold-Kalman order tracking filter formulates order extraction as a constrained estimation problem in which one (or multiple) rotation-synchronous components are tracked with high resolution even under rapid speed changes [6, 12]. For a target order κ_0, the measured signal is modeled as

$$x(t_n) = \Re\left\{a(t_n)\, e^{j\kappa_0\phi(t_n)}\right\} + \varepsilon(t_n), \quad n = 0,\ldots,N-1, \tag{32}$$

with slowly varying complex envelope $a(t)$, known phase $\phi(t)$ from the rotational reference and noise $\varepsilon(t)$. In vector formulation, VKF estimates the envelope samples

$$\mathbf{a} = (a(t_0),\ldots,a(t_{N-1}))^{\top} \in \mathbb{C}^N \tag{33}$$

by balancing data fidelity with an explicit smoothness constraint: Using the analytic representation

$$\mathbf{x}_a = \mathbf{x} + j\,\mathscr{H}(\mathbf{x}) \in \mathbb{C}^N \tag{34}$$

of

$$\mathbf{x} = (x(t_0),\ldots,x(t_{N-1}))^{\top}, \tag{35}$$

VKF solves the regularized least-squares problem

$$\hat{\mathbf{a}} = \arg\min_{\mathbf{a}} \left\|\mathbf{x}_a - \mathbf{H}(\phi)\,\mathbf{a}\right\|_2^2 + \lambda \left\|\mathbf{D}\,\mathbf{a}\right\|_2^2. \tag{36}$$

Here $\mathscr{H}(\cdot)$ denotes the Hilbert transform operator applied to $\mathbf{x}$ and $\mathbf{H}(\phi) \in \mathbb{C}^{N\times N}$ is diagonal,

$$\mathbf{H}(\phi) = \mathrm{diag}\big(e^{j\kappa_0\phi(t_0)}, \ldots, e^{j\kappa_0\phi(t_{N-1})}\big). \tag{37}$$

Moreover, $\mathbf{D} \in \mathbb{R}^{(N-2)\times N}$ is a difference operator enforcing smoothness (e.g., penalizing the second difference of the envelope, applied identically to real and imaginary parts), and λ controls the effective tracking bandwidth [6]. Larger values of λ enforce smoother envelopes and thus a narrower effective bandwidth. The resulting normal equations are sparse/banded and can be solved efficiently. Multi-order VKF tracks several orders simultaneously by stacking envelopes and corresponding blocks in $\mathbf{H}$; second-generation formulations explicitly address close and crossing orders [12]. Finally, the order-tracked time signal is reconstructed as

$$\hat{x}(t_n) = \Re\left\{\hat{a}(t_n)\, e^{j\kappa_0\phi(t_n)}\right\}. \tag{38}$$

In contrast to COT, VKF directly yields narrowband order signals in the time domain, with bandwidth largely independent of the speed sweep rate, making it a strong baseline for high-resolution order isolation under non-stationary operating conditions [6, 12].

3.2 Proposed method

For a fixed number $L \in \mathbb{N}$ with $L \geq 1$, we begin by creating overlapping intervals

$$[t_{a_i}, t_{a_i+l_i}] \subseteq [0,T], \qquad i = 0, \ldots, B-1, \tag{39}$$

on the discrete sampling grid $t_n = n/f_s$, $a_i, a_i + l_i \in \{0, \ldots, N-1\}$, $l_i \in \mathbb{N}$. The indices are chosen such that the following inequalities hold for the (approximated) accumulated rotational phase:

$$\phi(t_{a_i+l_i+1}) - \phi(t_{a_i}) > 2\pi L, \qquad \phi(t_{a_i+l_i}) - \phi(t_{a_i}) \leq 2\pi L, \qquad \phi(t_{a_{i+1}}) - \phi(t_{a_i}) \leq \pi L. \tag{40}$$

Consequently, we segment the sampled data into overlapping blocks of approximately L revolutions by choosing each block end $t_{a_i+l_i}$ such that the accumulated phase increment is maximal without exceeding $2\pi L$, and by advancing consecutive block starts by at most πL in the angle domain (i.e., at least 50% overlap). Moreover, since ϕ is continuous and strictly increasing, there exists $\tau_i \in [t_{a_i+l_i}, t_{a_i+l_i+1}]$ such that

$$\phi(\tau_i) - \phi(t_{a_i}) = 2\pi L, \tag{41}$$

and therefore $[t_{a_i}, t_{a_i+l_i}] \subseteq [t_{a_i}, \tau_i]$.

For each of the segments $[t_{a_i}, \tau_i]$, we tackle the order tracking problem as follows. Let

$$\xi : [\Phi_0, \Phi_0 + \Phi] \to \mathbb{R} \tag{42}$$

be a piecewise $\mathscr{C}^1$-function and consider its Φ-periodic extension. Then the Fourier coefficients

$$c_k = \frac{1}{\Phi} \int_{\Phi_0}^{\Phi_0+\Phi} \xi(\varphi)\, e^{-j2\pi k\varphi/\Phi}\, d\varphi, \qquad k \in \mathbb{Z}, \tag{43}$$

define the Fourier series

$$\sum_{k=-\infty}^{\infty} c_k \, e^{j\,2\pi k\varphi/\Phi}, \tag{44}$$

which converges to $\xi(\varphi)$ at every point of continuity and to the midpoint value at jump discontinuities. Since ϕ is strictly increasing, we are able to define ξ via

$$x(t) \triangleq \xi(\phi(t)), \quad t \in [t_{a_i}, \tau_i] \tag{45}$$

Then, by setting $\varphi = \phi(t)$, $\Phi_0 = \phi(t_{a_i})$ and $\Phi = 2\pi L$, we realize that the Fourier series Equation 44,

$$\sum_{k=-\infty}^{\infty} c_k \, e^{j\,\frac{k}{L}\phi(t)} = \Re\left\{ \sum_{k=0}^{\infty} 2c_k \, e^{j\,\frac{k}{L}\phi(t)} \right\}, \tag{46}$$

becomes the expansion of $x(t)$ into all non-negative rational orders with denominator L. Consequently, the half-bandwidth of this method is by design $\Delta\kappa = \frac{1}{2L}$. Usually integrals like Equation 43,

$$c_k = \frac{1}{2\pi L} \int_{\phi(t_{a_i})}^{\phi(t_{a_i})+2\pi L} \xi(\varphi) \, e^{-j\,\frac{k}{L}\varphi} \, d\varphi \tag{47}$$

are solved numerically by using an uniform grid together the rectangle rule, which results, by definition, in the DFT of ξ with respect to φ. Instead, we are using the non-uniform grid already at hand,

$$\phi(t_{a_i}), \phi(t_{a_i+1}), \ldots, \phi(t_{a_i+l_i-1}), \phi(t_{a_i+l_i}), \phi(t_{a_i}) + 2\pi L \tag{48}$$

and apply the trapezoidal rule:

$$\begin{aligned} c_k \approx & \frac{1}{4\pi L} \sum_{j=0}^{l_i-1} \left(x(t_{a_i+j}) \, e^{-j\,\frac{k}{L}\phi(t_{a_i+j})} + x(t_{a_i+j+1}) \, e^{-j\,\frac{k}{L}\phi(t_{a_i+j+1})} \right) \left(\phi(t_{a_i+j+1}) - \phi(t_{a_i+j}) \right) \\ & + \frac{1}{4\pi L} \left(x(t_{a_i+l_i}) \, e^{-j\,\frac{k}{L}\phi(t_{a_i+l_i})} + x(t_{a_i}) \, e^{-j\,\frac{k}{L}\phi(t_{a_i})} \right) \left(\phi(t_{a_i}) + 2\pi L - \phi(t_{a_i+l_i}) \right), \end{aligned} \tag{49}$$

For the i-th interval $[t_{a_i}, \tau_i]$, let c_k^i denote the right-hand side of Equation 49. Now, for each sample instant t_n, $n = 0, \ldots, N-1$, we determine the index set

$$I_n = \{ i \in \mathbb{N} : t_n \in [t_{a_i}, \tau_i] \} \tag{50}$$

of all segments t_n is contained in. For the target order κ_0, we then define the order-tracked signal of this method to be

$$\hat{x}(t_n) = \Re\left\{ \hat{a}(t_n) \, e^{j\,\kappa_0 \phi(t_n)} \right\}, \tag{51}$$

with

$$\hat{a}(t_n) = \frac{1}{\#I_n} \sum_{i \in I_n} 2c^i_{L\cdot\kappa_0}. \tag{52}$$

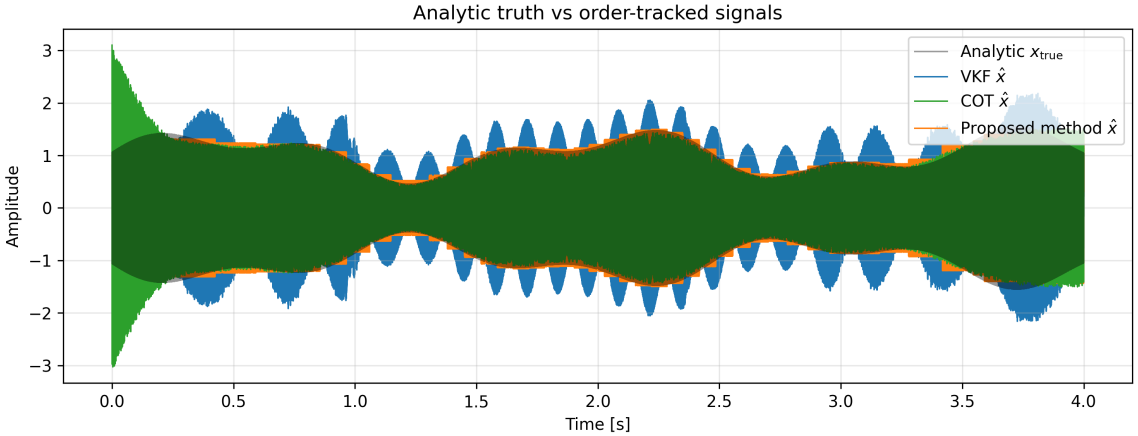

Figure 1: Time-domain comparison of the analytic ground-truth order component $x_{\text{true}}(t)$ and the extracted signals obtained using VKF, COT and the proposed method.

3.3 Results

Qualitative time-domain comparison

Figure 1 compares the order-tracked signals obtained using single-order VKF, COT and the proposed method with the analytic ground truth $x_{\text{true}}(t)$. Apart from its piecewise constant amplitudes, the proposed method closely matches the reference signal over the full duration of the run-up and run-down, with no visibly discernible distortion. In contrast, VKF exhibits residual oscillatory structure superimposed on the target order, consistent with envelope bias and partial suppression of nearby-order interference. The COT-based extraction shows pronounced transient artifacts at the beginning of the signal and visible amplitude distortions during periods of rapid speed variation.

Residual error structure

The corresponding residual errors

$$e(t) = \hat{x}(t) - x_{\text{true}}(t) \tag{53}$$

are shown in Figure 2. The proposed method maintains residuals close to zero throughout most of the signal duration, indicating effective suppression of interfering components and noise. VKF residuals exhibit increased variance and broadband structure, while COT residuals contain strongly structured components, particularly near the beginning and end of the signal and during nonstationary operating conditions.

Sensitivity to speed transients

Figure 3 shows the sliding RMS of the residual error (150 ms window) together with the instantaneous RPM signal. The RMS error of COT is correlated with rapid RPM changes, demonstrating its sensitivity to speed transients under nonstationary operation. VKF achieves a more

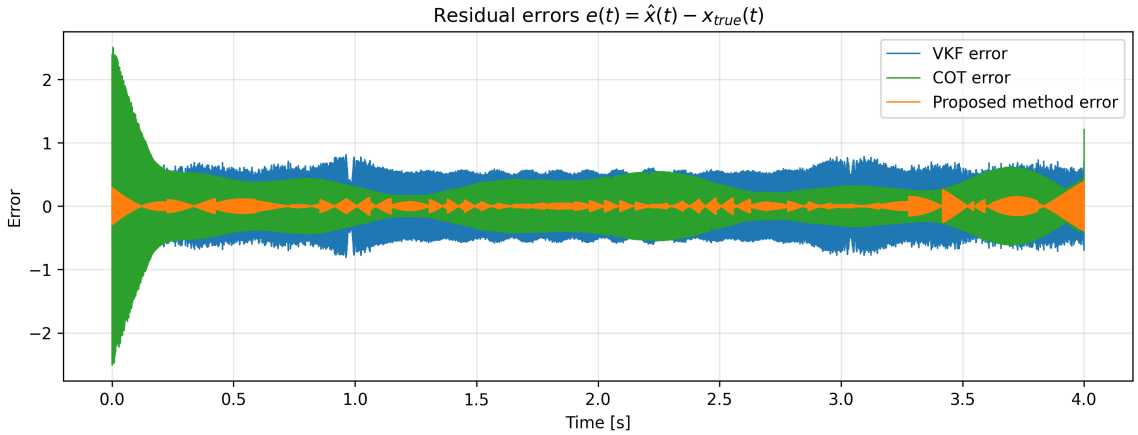

Figure 2: Residual errors $e(t) = \hat{x}(t) - x_{\text{true}}(t)$ for VKF, COT and the proposed method. Structured residuals indicate leakage or envelope distortion, whereas low-amplitude residuals indicate improved order isolation.

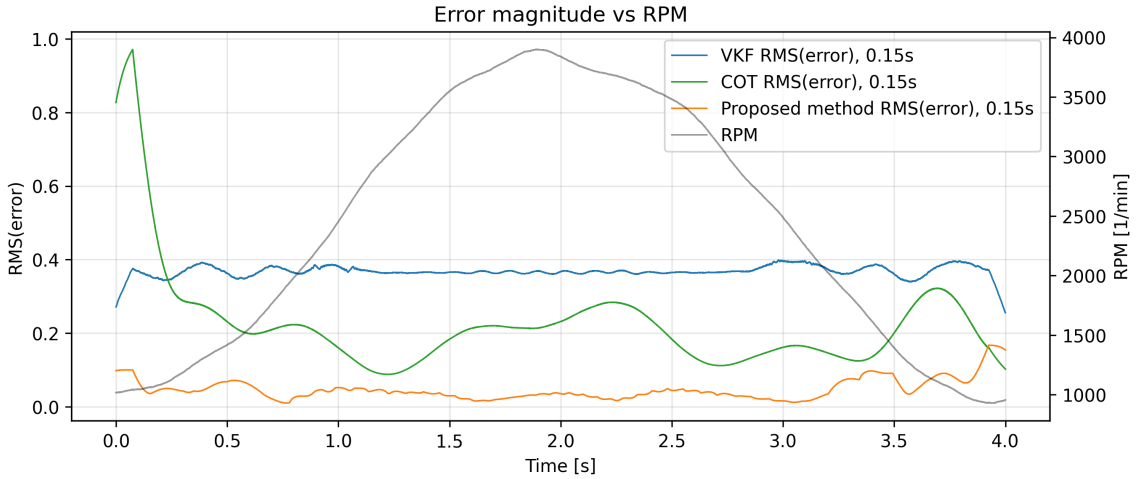

Figure 3: Sliding RMS of the residual error (150 ms window) for VKF, COT and the proposed method, plotted together with the instantaneous RPM (secondary axis). This diagnostic highlights the sensitivity of each method to speed transients.

uniform error level, but at a higher baseline magnitude. In contrast, the proposed method maintains a low error magnitude with only weak dependence on RPM slew rate, including during the sharp transient around the mid-run.

Envelope accuracy

Envelope amplitude and phase diagnostics for the target order are shown in Figure 4. After alignment to remove the global complex scaling ambiguity, VKF is observed to attenuate and distort faster envelope variations and exhibits large, localized phase excursions. COT preserves envelope phase more accurately than VKF but shows amplitude bias and transient overshoot.

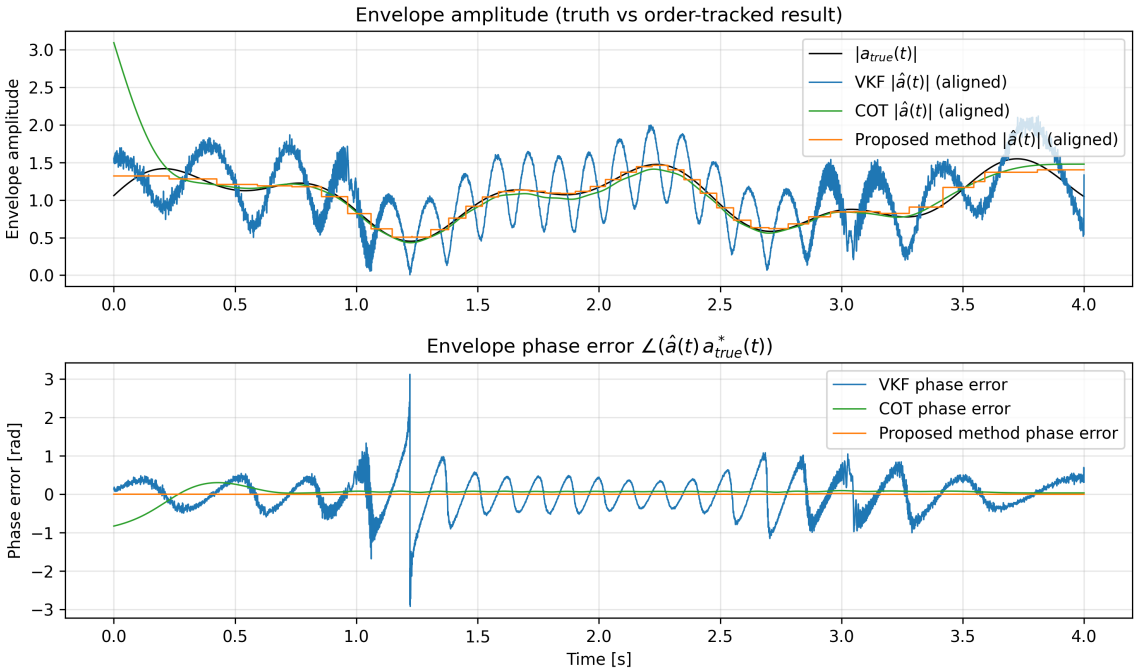

Figure 4: Envelope diagnostics for the target order. ***Top:*** *Envelope amplitude $|a(t)|$ for analytic ground truth and aligned estimates.* ***Bottom:*** *Envelope phase error $\angle(\hat{a}(t)a^*_{\text{true}}(t))$ for VKF, COT and the proposed method.*

The proposed method closely follows both the amplitude and phase of the analytic envelope over the entire signal duration, resulting in substantially reduced envelope errors.

Quantitative error metrics

Quantitative error metrics against the analytic ground truth confirm the qualitative observations. The proposed method achieves a signal-to-error ratio of 22.5 dB, compared to 8.8 dB for COT and 6.4 dB for VKF, along with a near-perfect correlation coefficient of 0.998. Envelope amplitude and phase errors are reduced by more than an order of magnitude relative to both baseline methods.

Block-wise spectral error

The proposed method segments the sampled signal into overlapping blocks, and the order-tracking problem is solved independently on each block. Importantly, this segment-wise processing is not intended to reconstruct a time-domain signal over the entire measurement duration; the reconstructed signal shown in Fig. 1 is used solely for benchmarking and comparison against state-of-the-art baselines. The primary objective of the proposed approach is instead to obtain block-localized order representations that admit accurate short-time Fourier transforms, which can be combined across blocks to form cross-spectral matrices for (advanced) frequency-domain beamforming.

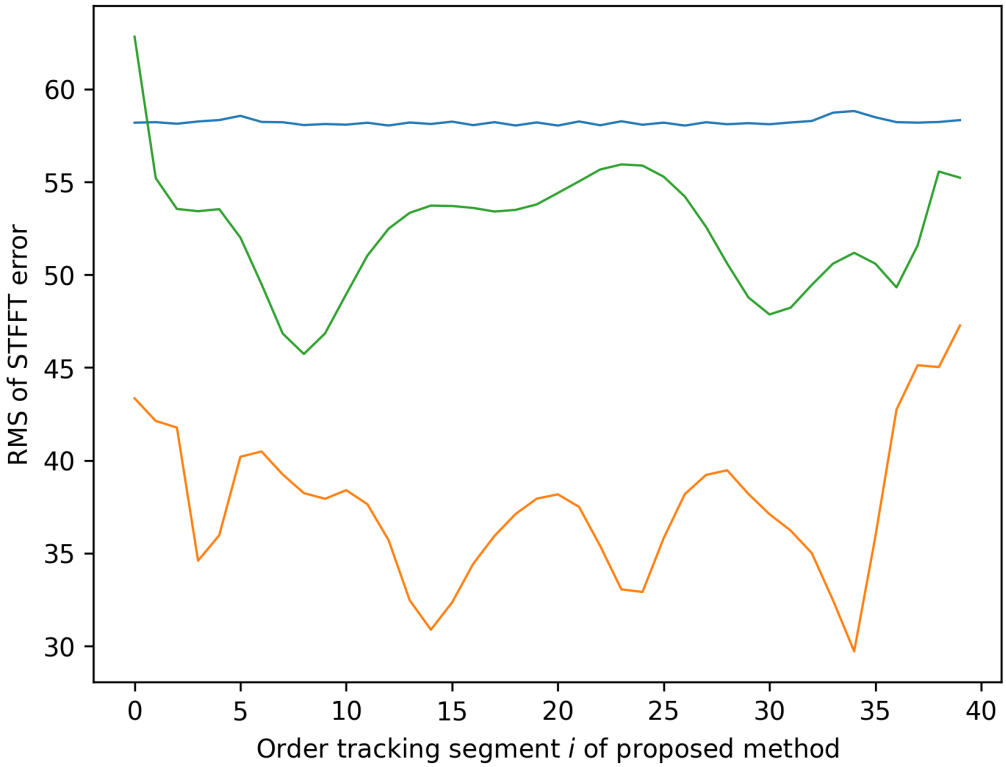

Figure 5: Block-wise RMS of STFFT error of the extracted target-order signal for VKF, COT and the proposed method. Blocks are aligned with the phase-domain segmentation. Lower values indicate improved spectral fidelity.

Figure 5 therefore evaluates the accuracy of the block-wise spectral representation directly. For each block, an STFFT is computed on the order-tracked signal restricted to that block, and the resulting spectrogram is compared against the corresponding ground-truth spectrogram. More precisely, we compute the RMS of the difference between these two spectrograms. This procedure avoids the artificial discontinuities that would arise if a continuous time-domain signal were first reconstructed and subsequently re-segmented for STFFT analysis.

The proposed method consistently attains lower block-wise spectral error across nearly all blocks, indicating that its block-local order representations closely match the true spectral content within each phase-aligned segment. COT exhibits pronounced block-to-block variability, reflecting sensitivity to local speed variations and order leakage, while VKF yields more uniform errors at a systematically higher level. These results demonstrate that the proposed method provides a more accurate and robust block-wise spectral representation, which is critical for subsequent frequency-domain processing such as beamforming.

Runtime benchmarking

To assess computational efficiency, we benchmarked all methods on the same nontrivial simulation instance, tracking a set of five neighboring orders $\{98, 99, 100, 101, 102\}$ over our four-second signal. Each method was executed repeatedly using high-resolution wall-clock timing,

with a short warm-up phase and explicit garbage-collection between runs to minimize measurement bias.

Single-order VKF was applied independently to each requested order, resulting in a total runtime that scales linearly with the number of extracted orders. For this multi-order benchmark, VKF required on average 2.45 s per execution, reflecting the cost of solving a large, regularized linear system for each order.

In contrast, COT and the proposed method exhibit substantially lower execution times. COT required 0.051 s on average, while the proposed method required 0.054 s, with comparable variance across repeated runs. Despite the use of block-wise processing and additional logic for phase-domain segmentation, the proposed method achieves runtime performance on par with COT and more than an order of magnitude faster than single-order VKF in this multi-order setting.

4 Order-selective beamforming

4.1 Time-domain beamforming with revolution-synchronous resampling (TDBF-OT)

A common state-of-the-art baseline performs beamforming directly in the time domain and applies order tracking only after spatial focusing. In this approach, a delay-and-sum beamformer is first applied independently at each scan point to produce a scalar beamformed time signal [10]. To account for variable rotational speed, this signal is subsequently resampled with respect to the measured rotational reference, yielding a revolution-synchronous representation in which rotation-synchronous components become stationary [5].

Map values are then derived from the resampled beamformer output, typically through RMS averaging (over a fixed number of revolutions). If order-selective maps are desired, additional order-domain filtering can be applied prior to the averaging step, since orders appear as stationary components in the revolution domain.

In contrast to the method presented in subsection 4.2, which performs order-selective processing prior to cross-spectral-matrix construction and operates directly on the multi-channel data, the present baseline applies order tracking only to the scalar beamformer output. Nevertheless, TDBF-OT serves as a strong and widely adopted reference for evaluating order-related beamforming performance under nonstationary operating conditions [10].

4.2 Order-selective pre-CSM-filtering using the proposed method (OS-FDBF)

Building on the block-wise processing framework described previously (cf. subsection 3.2), the proposed method naturally enables order-selective pre-filtering prior to cross-spectral matrix (CSM) construction. For each accumulated-phase-aligned block of subsection 3.2, one or multiple target orders are extracted locally, and short-time Fourier transforms (STFFTs) are computed directly on the corresponding block-local order representations. The block-wise CSM is then formed by accumulating the cross-spectral products across microphones and STFFT blocks.

This procedure performs order-selective filtering before CSM construction, ensuring that the resulting spatial statistics are dominated by the orders of interest while reducing contamination from neighboring orders, broadband noise and non-synchronous disturbances. Since the CSM

is assembled from block-local spectral representations, artificial discontinuities that would arise from reconstructing and re-segmenting a continuous time-domain signal are avoided.

Once the order-selective CSM has been constructed, the proposed framework is fully compatible with a wide range of established frequency-domain array processing methods. In particular, the CSM can be used directly as input to conventional and advanced beamforming techniques such as standard beamforming, MUSIC [4], CLEAN-SC [11], DAMAS (e.g. [1]) and functional or power beamforming approaches (e.g. [2, 7]). Importantly, the proposed method imposes no restrictions on the number of orders considered or on the subsequent spatial processing stage; instead, it provides a flexible and accurate order-selective spectral representation that can be exploited by any CSM-based frequency-domain method.

4.3 Acoustic maps

Simulation

To evaluate the proposed order-selective pre-CSM filtering (OS-FDBF) approach, a controlled acoustic simulation was conducted using a circular array of 32 microphones with a diameter of 0.7 m (Fig. 6a). Two stationary point sources of equal sound pressure level (60 dB) were placed at a distance of 1 m from the array center at positions $(-0.2\,\mathrm{m}, 0\,\mathrm{m})$ and $(0.2\,\mathrm{m}, 0\,\mathrm{m})$. The sources emit rotation-synchronous components corresponding to orders $\kappa = 60$ and $\kappa = 72$, respectively, driven by a linear RPM ramp from 1000 rpm to 2000 rpm over 1 s (Fig. 6b).

The order spectrum (Fig. 6c) shows two distinct components at $\kappa = 60$ and $\kappa = 72$, confirming that the sources are well separated in the order domain. In contrast, the frequency spectrum (Fig. 6d) exhibits strong spectral smearing caused by the nonstationary excitation, leading to substantial overlap between the sources. This demonstrates that frequency-domain processing alone is insufficient for reliable separation.

The beamforming results obtained using the conventional TDBF-OT baseline are shown in Fig. 7. In both cases, the sources are correctly localized but their levels are systematically underestimated by approximately 5 dB. Moreover, the results exhibit visible spatial artefacts.

For the proposed OS-FDBF method, the beamforming maps shown in Fig. 8 are computed using standard beamforming over a frequency range corresponding to the smeared order components (i.e. the combined third-octave bands from 1 kHz to 2.5 kHz), thereby integrating spectral contributions over the entire nonstationary time interval.

In contrast to the baseline, the proposed approach recovers both source locations with high accuracy and reconstructs their levels close to the true 60 dB. Moreover, the resulting maps are significantly smoother and largely free of artefacts.

Notably, the selection of the frequency range in OS-FDBF implicitly determines the portion of the nonstationary signal that contributes to the CSM. Since frequency corresponds to different time instances under varying rotational speed, selecting different frequency bands effectively allows traversal through the time evolution of the signal. This provides additional flexibility compared to conventional approaches, enabling targeted analysis of specific operating conditions within the measurement.

Overall, while both methods successfully localize the sources, the proposed OS-FDBF approach achieves superior level accuracy and improved spatial map quality for the chosen simulation.

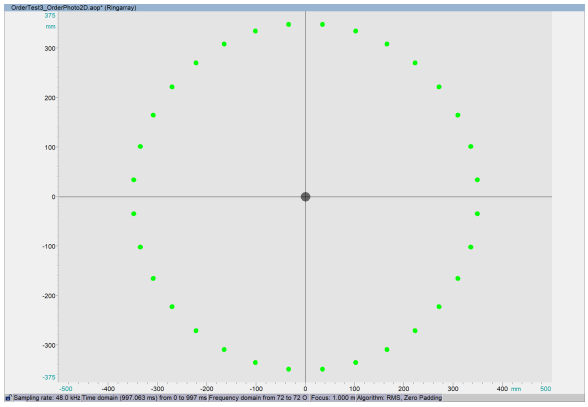

(a) Array geometry

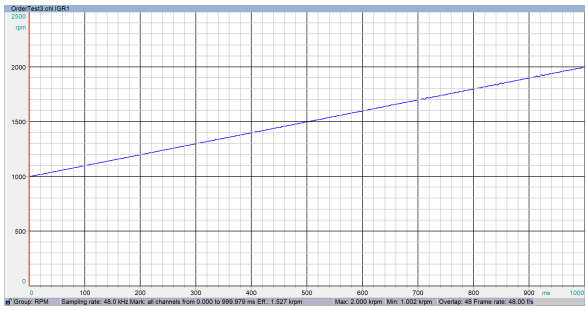

(b) RPM signal

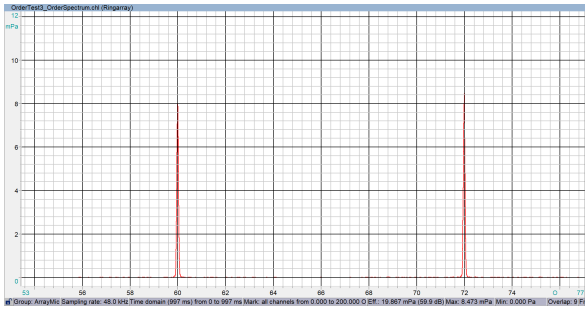

(c) Order spectrum

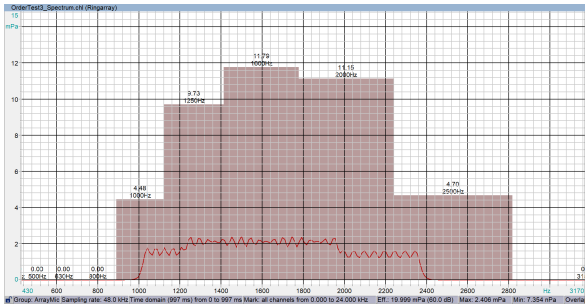

(d) Frequency spectrum

Figure 6: Array setup and signal characteristics. In the order domain, both sources are clearly separated, while in the frequency domain their contributions are strongly smeared and overlap due to the nonstationary RPM ramp.

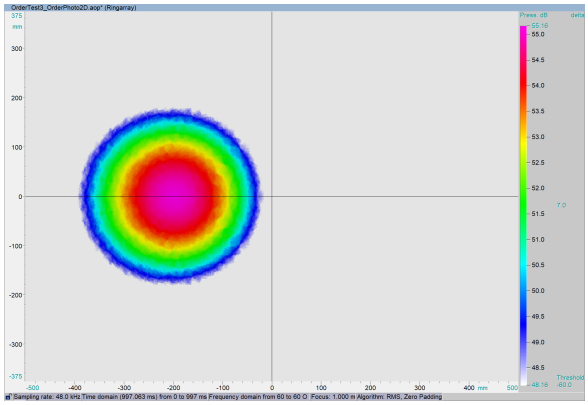

(a) Order $\kappa = 60$

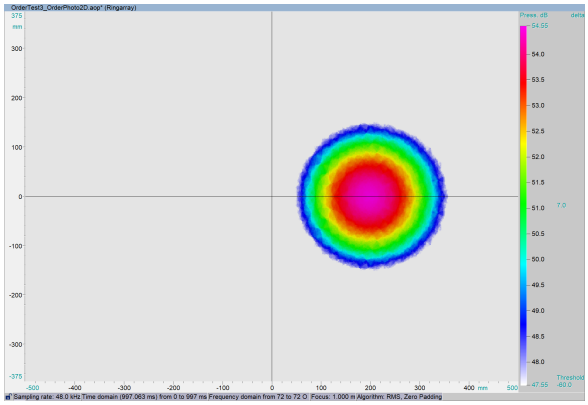

(b) Order $\kappa = 72$

Figure 7: Beamforming maps obtained using TDBF-OT. Sources are correctly localized but exhibit approximately 5 dB *level underestimation and noticeable artefacts.*

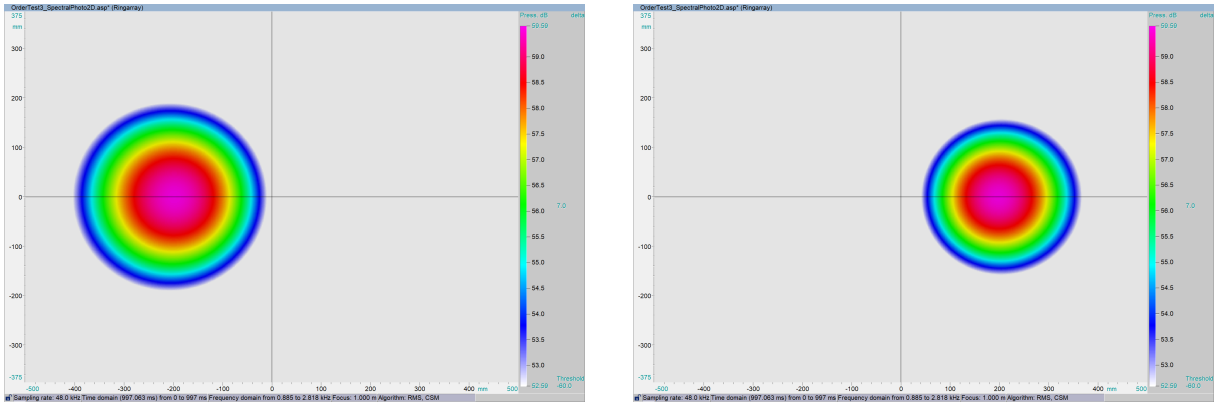

(a) Order $\kappa = 60$ *(b) Order $\kappa = 72$*

Figure 8: Beamforming maps obtained using the proposed OS-FDBF method combined with standard beamforming. Both sources are accurately localized with nearly correct level reconstruction and smooth, artefact-free spatial distributions.

Real-world measurement: Motor run-up

To validate the proposed method under realistic conditions, a motor run-up measurement was investigated using a circular array of 32 microphones placed at a distance of approximately 1 m from the source (Fig. 9a). The array geometry is overlaid on an optical image of the setup to provide spatial reference. The rotational speed varies slowly from approximately 3940 rpm to 4040 rpm over a duration of 1.6 s (Fig. 9b), corresponding to a nearly stationary operating condition.

The corresponding broadband frequency spectrum (Fig. 9d) shows energy distributed across a wide frequency range, making direct interpretation in the frequency domain challenging. The order spectrum (Fig. 9c) reveals a highly irregular and spiky structure, indicating multiple acoustic order contributions of comparable magnitude. In the following, the component at order $\kappa = 45$ is considered to serve as an example.

As a baseline, time-domain beamforming with revolution-synchronous resampling (TDBF-OT) is applied. Again, for comparison, we consider the proposed order-selective pre-CSM filtering (OS-FDBF) approach. In this case, to avoid explicit tracking of the instantaneous order frequency, the CSM is constructed over a fixed broadband frequency range from 0 to 5 kHz.

The resulting beamforming maps (Fig. 10) appear qualitatively similar for both approaches. Multiple regions of elevated sound pressure are observed, suggesting the presence of several sources of comparable strength. Although the OS-FDBF result exhibits slightly improved smoothness and level consistency, the overall interpretation of the maps remains largely unchanged. At this stage, a conventional evaluation would suggest a distributed set of sources.

However, this conclusion may be misleading. The observed spatial structures may be dominated by sidelobe artefacts rather than true physical sources. To resolve this ambiguity, the same CSM is processed using CLEAN-SC.

The CLEAN-SC results in Fig. 11 clearly indicate that most of the apparent sources in Fig. 10 correspond to sidelobes. Only a small number of dominant source regions remain after deconvolution. The representation using a 7 dB dynamic range highlights the strongest contributions

(a) Measurement setup

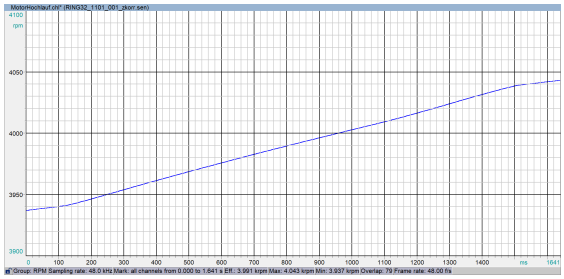

(b) RPM signal

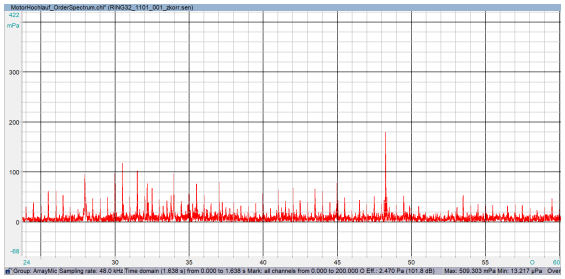

(c) Order spectrum

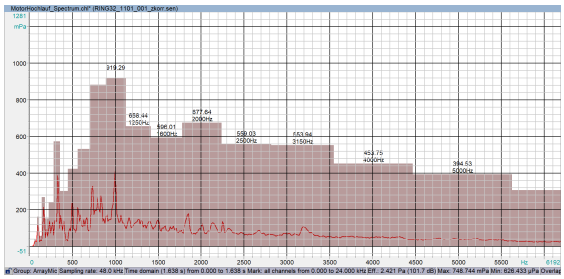

(d) Frequency spectrum

Figure 9: Real-world measurement: Measurement setup, RPM signal and spectral representations. The order spectrum exhibits a complex multi-source structure, while the frequency domain shows broadband energy distribution.

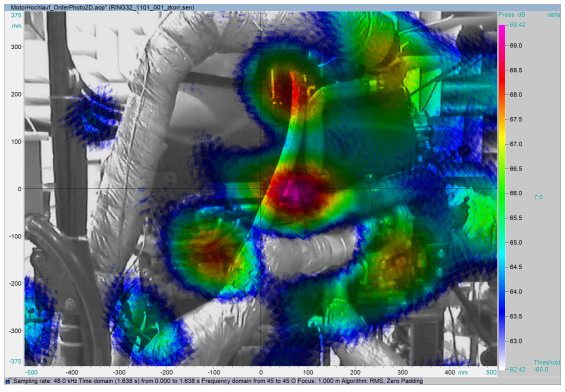

(a) TDBF-OT

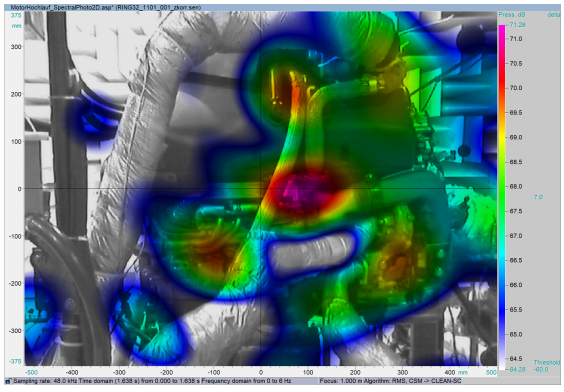

(b) OS-FDBF (standard beamforming)

Figure 10: Beamforming results for order $\kappa = 45$. Both methods produce similar maps with multiple apparent sources, making interpretation ambiguous.

and makes it directly comparable to the standard beamforming results, while the 15 dB visualization provides additional detail on weaker components.

These results demonstrate that conventional beamforming, even when visually interpretable, can lead to incorrect conclusions in complex measurement scenarios. In contrast, the proposed

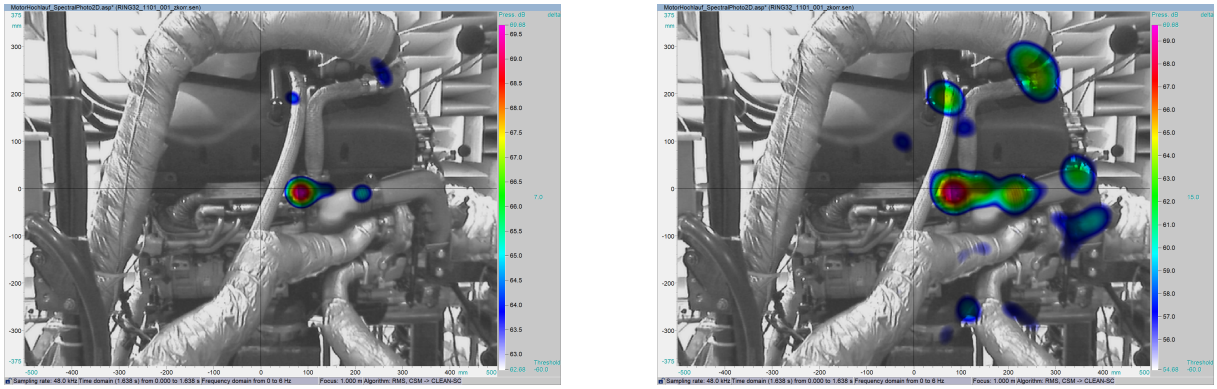

(a) Dynamic range 7 dB *(b) Dynamic range* 15 dB

Figure 11: Beamforming results using OS-FDBF combined with CLEAN-SC. Deconvolution suppresses sidelobes and reveals the underlying source structure.

OS-FDBF approach, when combined with CSM-based deconvolution methods such as CLEAN-SC, enables a more reliable and physically meaningful separation of true sources from artefacts.

Importantly, OS-FDBF does not require prior knowledge of the instantaneous order frequency in the frequency domain. By constructing the CSM over an appropriately chosen broadband interval, the relevant contributions of the nonstationary order are inherently captured, allowing robust subsequent frequency-domain processing.

Acknowledgements

This research has been funded by German Federal Ministry for Economic Affairs and Climate Action (Bundesministerium für Wirtschaft und Klimaschutz BMWK) under project *KadoS* registration number 49MF230110.

References

[1] T. F. Brooks and W. M. Humphreys. “A deconvolution approach for the mapping of acoustic sources (DAMAS) determined from phased microphone arrays.” *Journal of Sound and Vibration*, 294(4–5), 856–879, 2006. doi:10.1016/j.jsv.2005.12.046.

[2] R. P. Dougherty. “Functional beamforming.” In *Proceedings on CD of the 5th Berlin Beamforming Conference, 19-20 February 2014*. GFaI, Gesellschaft zu Förderung angewandter Informatik e.V., Berlin, 2014. ISBN 978-3-942709-12-5. URL `http://bebec.eu/Downloads/BeBeC2014/Papers/BeBeC-2014-01.pdf`.

[3] K. R. Fyfe and E. D. Munck. “Analysis of computed order tracking.” *Mechanical Systems and Signal Processing*, 11(2), 187–205, 1997. doi:10.1006/mssp.1996.0076.

[4] D. H. Johnson and D. E. Dudgeon. *Array Signal Processing, Concepts and Techniques*. P T R Prentice Hall, Englewood Cliffs, 1993.

[5] S. J. Orfanidis. *Introduction to Signal Processing*. Prentice Hall, Upper Saddle River, NJ, 1996.

[6] M.-C. Pan and Y.-F. Lin. "Further exploration of Vold-Kalman-filtering order tracking with shaft-speed information—I: Theoretical part, numerical implementation and parameter investigations." *Mechanical Systems and Signal Processing*, 20(5), 1134–1154, 2006. doi:10.1016/j.ymssp.2005.01.005.

[7] C. Puhle. "Demonstration of a unified approach to beamforming." In *Proceedings of 50th International Congress and Exposition on Noise Control Engineering (INTERNOISE 2021)*. August 2021, Washington DC, USA.

[8] R. B. Randall. *Vibration-Based Condition Monitoring: Industrial, Aerospace and Automotive Applications*. John Wiley & Sons, Chichester, UK, 2011. doi:10.1002/9780470977668.

[9] P. N. Saavedra and C. G. Rodriguez. "Accurate assessment of computed order tracking." *Shock and Vibration*, 13(1), 13–32, 2006. doi:10.1155/2006/838097. URL `https://onlinelibrary.wiley.com/doi/epdf/10.1155/2006/838097`.

[10] S. Schmidt. "Reducing beamforming calculation time with GPU accelerated algorithms." In *Proceedings on CD of the 5th Berlin Beamforming Conference, 19-20 February 2014*. GFaI, Gesellschaft zu Förderung angewandter Informatik e.V., Berlin, 2014. ISBN 978-3-942709-12-5. URL `http://bebec.eu/Downloads/BeBeC2014/Papers/BeBeC-2014-08.pdf`.

[11] P. Sijtsma. "CLEAN based on spatial source coherence." In *13th AIAA/CEAS Aeroacoustics Conference, May 21-23*. AIAA Paper 2007-3436, 2007.

[12] H. Vold, M. Mains, and J. R. Blough. "Theoretical foundations for high performance order tracking with the Vold-Kalman tracking filter." In *SAE Technical Paper*. SAE International, Warrendale, PA, 1997. Available via JSTOR.

[13] C. Zhang, R. Wang, L. Yu, and Y. Xiao. "Order domain beamforming for the acoustic localization of rotating machinery under variable speed working conditions." *Applied Acoustics*, 205, 109290, 2023. doi:10.1016/j.apacoust.2023.109290.